Variational Integrators and the Three-Body Problem

Evan Gawlik

Abstract

This study applies variational integrators to the three-body problem, a classic problem from celestial mechanics that asks for the motion of three masses in space under mutual gravitational interaction. The use of variational integrators, a class of numerical methods used to simulate mechanical systems, is of value because they are known to exhibit accurate behavior with respect to the preservation of physical constants of motion when applied to systems with conserved quantities like energy and momentum. This contrasts with the performance of other numerical differential equation-solving algorithms like the Runge-Kutta method, which typically experience artificial dissipation of conserved quantities over successive iterations. A comparison of the performance of variational integrators versus the fourth-order Runge-Kutta method applied to the planar circular restricted three-body problem composes the core of this study. In particular, the algorithms are evaluated based on their ability to accurately model individual trajectories, conserve integrals of motion, predict statistical quantities like transport rates, and preserve the structure of Poincaré section plots. In addition to the contributing to the development of numerical methodology, these investigations have applications to solar system simulations and to the design of spacecraft mission trajectories.

1 Introduction

Predicting the motion of a set of bodies in space under mutual gravitational interaction is a classic problem in the study of celestial mechanics. Consider n masses m_i whose motions $\mathbf{r}_i(t)$ are determined by gravitational forces. From Newton's laws, the differential equations of motion for these bodies are

$$m_i \ddot{\mathbf{r}}_i(t) = \sum_{j \neq i} \frac{G m_i m_j}{r_{ij}^2} \hat{\mathbf{r}}_{ij}, \tag{1}$$

where G is the universal gravitational constant and $\mathbf{r}_{ij} = \mathbf{r}_j - \mathbf{r}_i$. The n-body problem entails finding each body's position as a function of time given the initial positions and initial velocities of the n masses. For the case of two masses, a general solution can be found analytically[1]. For $n \geq 3$, the problem permits no general solution, even in the restricted case of a test mass moving in the orbital plane of two circularly orbiting primaries (the planar circular restricted three-body problem [PCR3BP])[2]. It comes as no surprise then that numerical methods play a vital role in studying celestial mechanical problems. Likewise, the PCR3BP is an ideal choice for a test bed upon which a comparison of numerical methods can be made, owing to both its simple formulation and its interesting dynamics.

1.1 Numerical methods

This study focuses on the application of variational integrators to the PCR3BP. The use of variational integrators, a class of numerical methods used to simulate mechanical systems, is of value because they are known to exhibit accurate behavior with respect to the preservation of physical constants of motion when applied to systems with conserved quantities like energy and momentum[3]. They arise from approaching

mechanical systems from a variational mechanics standpoint. Particularly, a fundamental principle from classical mechanics states that a mechanical system will evolve such that the so-called action integral

$$\int_0^T L(q(t), \dot{q}(t)) \, \mathrm{d}t \tag{2}$$

is extremized subject to fixed endpoints $q(0)$ and $q(T)$, where q is a generalized coordinate vector and $L(q(t), \dot{q}(t))$ is the system's kinetic energy minus potential energy at time t. Calculus of variations then shows that this holds only if $q(t)$ satisfies the Euler-Lagrange equations:

$$\frac{\partial L}{\partial q} - \frac{\mathrm{d}}{\mathrm{d}t} \frac{\partial L}{\partial \dot{q}} = 0. \tag{3}$$

As an example, consider a particle moving in $\mathbb{R}^3$ in the presence of a potential $V(q)$, where q is the usual cartesian position vector (x, y, z). Then $L = \frac{1}{2}\dot{q}^T M\dot{q} - V(q)$ and equation (3) reduces to Newton's second law, force equals mass times acceleration:

$$M\ddot{q} = -\nabla V(q). \tag{4}$$

To derive a variational integrator, one discretizes the action integral (2) and uses a discrete version of the Euler-Lagrange equations (3) to define a map $(q_{k-1}, q_k) \mapsto (q_k, q_{k+1})$, where $q_k \approx q(kh)$ and h is a time step. This map is then applied recursively to a set of initial conditions (q_0, q_1) to produce a discrete curve of points $\{q_k\}_{k=0}^{T/h}$ that approximates $q(t)$ over the time interval $[0, T]$. Different variational integrators, possibly with differing orders of accuracy, can be constructed using different quadrature methods for the discretization of the action integral (2)[4].

Two distinguishing features of constant time-stepping variational integrators applied to conservative mechanical systems are symplecticity (for systems with one degree of freedom, this property can be realized as preservation of area in phase space under the discrete Lagrangian map $(q_{k-1}, q_k) \mapsto (q_k, q_{k+1})$) and momentum conservation[5].

As a basis for comparison in this study, the results of applying variational integrators to the PCR3BP are compared with those arrived at through applying the fourth-order Runge-Kutta method[6], a popular numerical algorithm used to integrate ordinary differential equations of the form $\dot{q} = f(q, t)$. If the function f is time independent, the Runge-Kutta method takes the form

$$q_{k+1} = q_k + \frac{1}{6}a_1 + \frac{1}{3}a_2 + \frac{1}{3}a_3 + \frac{1}{6}a_4, \tag{5}$$

where

$$
\begin{aligned}
a_1 &= hf(q_k) \\
a_2 &= hf(q_k + \frac{1}{2}a_1) \\
a_3 &= hf(q_k + \frac{1}{2}a_2) \\
a_4 &= hf(q_k + a_3),
\end{aligned}
$$

which recursively generates a discrete curve of points $\{q_k\}_{k=0}^{T/h} \approx \{q(kh)\}_{k=0}^{T/h}$ from initial conditions q_0.

1.2 The planar circular restricted three-body problem (PCR3BP)

The PCR3BP considers the motion of a test mass $m_3 = 0$ in the presence of the gravitational field of two primary masses $m_1 = 1 - \mu$ and $m_2 = \mu$ in circular orbits about their center of mass. Without loss of generality, all units are normalized and positions are defined relative to a rotating coordinate frame whose x-axis coincides with the line joining m_1 and m_2 and whose origin coincides with the center of mass of m_1 and m_2, as shown in Fig. 1. The equations of motion for the test particle are then[2]
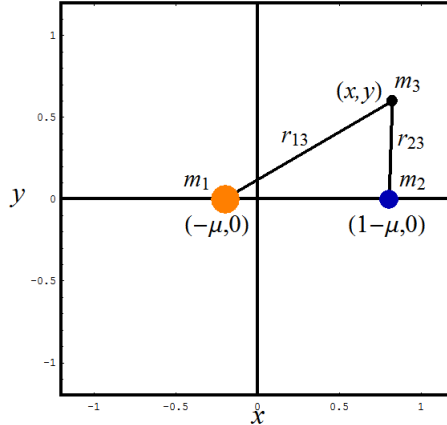
Figure 1: Rotating coordinate system in the planar circular restricted three-body problem. All units are nondimensionalized. The coordinate frame rotates counterclockwise with unit angular frequency.

$$\ddot{x} - 2\dot{y} = \frac{\partial \Omega}{\partial x} \tag{6}$$

$$\ddot{y} + 2\dot{x} = \frac{\partial \Omega}{\partial y}, \tag{7}$$

where

$$\Omega(x,y) = \frac{x^2 + y^2}{2} + \frac{1-\mu}{\sqrt{(x+\mu)^2 + y^2}} + \frac{\mu}{\sqrt{(x-1+\mu)^2 + y^2}} + \frac{1}{2}\mu(1-\mu) \tag{8}$$

and (x, y) denotes the position of m_3 in the rotating frame.

It is straightforward to check through differentiation that

$$C(x, y, \dot{x}, \dot{y}) = 2\Omega(x, y) - (\dot{x}^2 + \dot{y}^2) \tag{9}$$

is a constant of motion for this system. This value C is commonly referred to as the Jacobi integral[7]. We shall refer to the constant $E = -C/2$ as the energy of the system, taking care not to confuse E with the sum of the test particle's kinetic and potential energies.

In this study we choose a mass parameter $\mu = 9.537 \times 10^{-4}$, which corresponds to the mass ratio for the Sun and Jupiter[8]. Thus, solving the equations of motion (6-7) can be physically interpreted as simulating the motion of a small mass (e.g. a spacecraft or a comet) in the presence of the gravitational field of the Sun-Jupiter system.

2 Results

2.1 Individual trajectories

We begin with an evaluation of the performance of variational integrators and the Runge-Kutta method applied to calculating individual trajectories. Rather than attempting to survey a wide range of orbits corresponding to different initial conditions, we focus here an class of interesting trajectories called transit orbits.

Consider expression (9) for the Jacobi constant C. Since C is constant and $(\dot{x}^2 + \dot{y}^2)$ is a nonnegative quantity, it immediatelly follows that m_3 is restricted to regions of the (x, y) plane where

$$\Omega(x, y) \geq C/2. \tag{10}$$

An example of the allowed regions of motion for a system with a given Jacobi constant C and mass parameter μ is shown in Fig. 2(a). Notice that the example in Fig. 2(a) allows for transit orbits – trajectories that
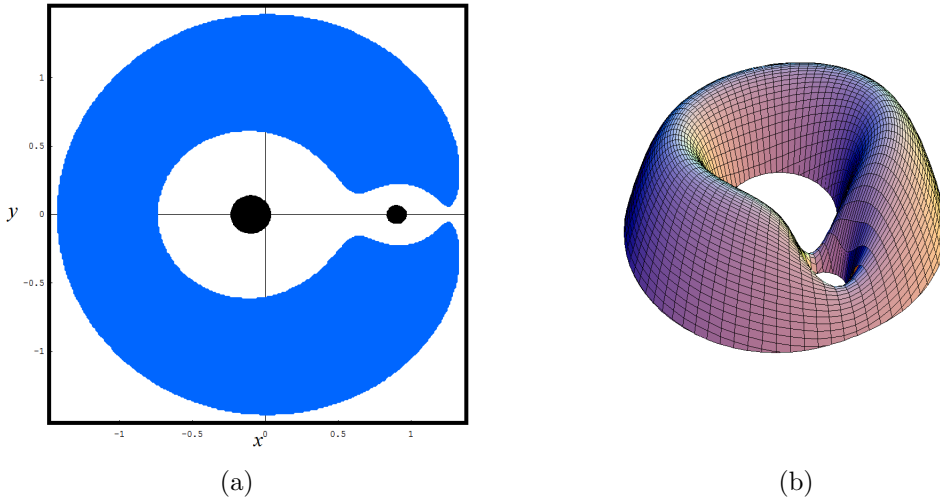
3

Figure 2: (a) Regions of allowed motion (white areas) in the planar circular restricted three-body problem with $\mu = 0.1$, $C = 3.55$. (b) Graph of the negative of the effective potential $\Omega(x, y)$.

transition between orbiting outside m_2's orbit (the exterior region) and orbiting inside m_2's orbit (the interior region). These types of orbits are mimicked in the solar system by comets such as *Oterma*, whose orbit in the past century has experienced a resonance transition between an exterior and interior orbit and back with respect to the Sun-Jupiter system[9]. An understanding of the dynamics of orbits like these can be applied, for example, to the design of low-fuel spacecraft mission trajectories[10]. For a thorough discussion of transit orbits and procedures for constructing initial conditions that generate transit orbits, see Koon *et al.*[8].

In Appendix Figs. 7 and 8, the results of the integration of two sets of transit orbit initial conditions obtained from Koon *et al.*[8] are shown. For small time steps, the methods agree on the two trajectories associated with the initial conditions. For larger time steps, the methods disagree. In the case of Appendix Fig. 7, the variational integrator predicts an orbit that differs qualitatively from the resolved calculation, while the Runge-Kutta method generates an orbit consistent with the resolved calculation. In Appendix Fig. 8, the opposite occurs: the variational integrator follows the benchmark calculation closely, while the Runge-Kutta method deviates significantly.

In general, comparing individual trajectories reveals few patterns that characterize the performance of variational integrators versus the Runge-Kutta method applied to the PCR3BP. As we have just observed, one can find cases in which a variational integrator appears to outperform the Runge-Kutta method in calculating a trajectory, and vice-versa. In the following two sections, we examine some properties that distinguish variational integrators from standard numerical methods.

2.2 Energy conservation

Preserving constants of motion in numerical simulations bears importance in a variety of physical situtations. A frictionless pendulum should oscillate infinitely with constant amplitude; an energy-conserving integrator will qualitatively reproduce this behavior, whereas a dissipative integrator will predict decaying oscillation. Naturally, good energy behavior is favorable when one seeks qualitative accuracy over long time spans.

For mechanical systems with conserved quantities that arise from symmetries of the system (e.g. invariance of the Lagrangian under translation or rotation), a discrete version of Noether's theorem from classical mechanics that guarantees exact conservation of the corresponding momenta (e.g. linear momentum and angular momentum) accompanies the use of a variational integrator[5]. Exact energy conservation, on the other hand, does not accompany the use of a constant time-stepping variational integrator for most systems of interest. Nonetheless, variational integrators are known to exhibit excellent energy behavior when applied
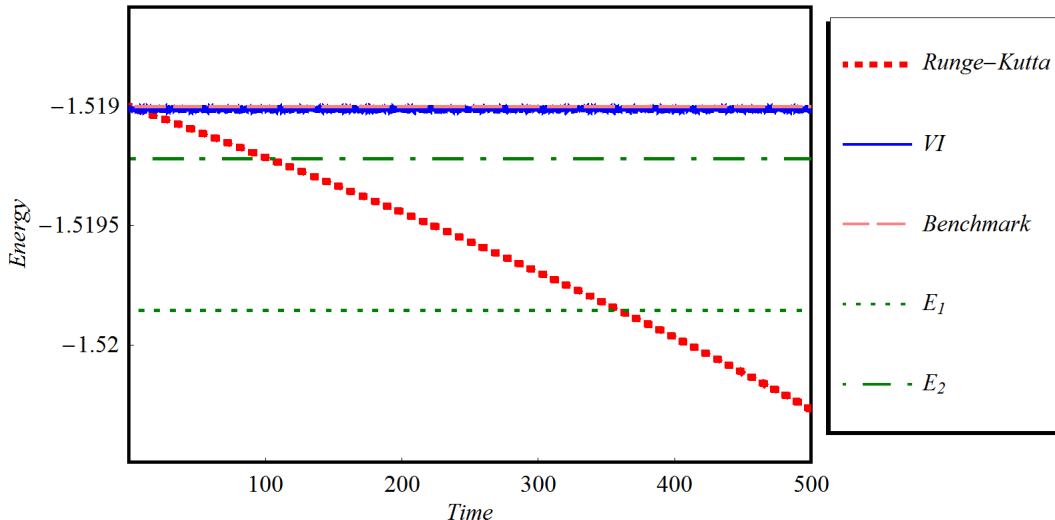
Figure 3: Energy vs. time for a direct (counterclockwise) orbit around m_2. E_1 and E_2 correspond to energy levels that separate different configurations of the forbidden regions, as shown in Appendix Fig. 6.

to conservative mechanical systems[3].

Fig. 3 shows the energy-conserving performance of a variational integrator compared to the Runge-Kutta algorithm applied to a direct (counterclockwise) orbit about m_2 with a time step $h = 0.015$. For reference, energy levels that correspond to critical values that separate different configurations of the forbidden regions are plotted. Notice that while the variational integrator energy oscillates about its initial value, the Runge-Kutta energy decreases almost linearly. Moreover, the Runge-Kutta method dissipates enough energy to lead to changes in the configuration of the allowed regions of motion. Appendix Fig. 6 displays the forbidden region configurations associated with these lower energy levels.

2.3 Poincaré section plots

It was mentioned previously that Koon *et al.*[8] outline a procedure for numerically constructing initial conditions that generate orbits with prescribed itineraries. It turns out that Poincaré sections play a key role in this process, allowing one to identify regions of phase space associated with selected trajectories. Likewise, Dellnitz *et al.*[11] demonstrate the power of identifing chaotic regions and resonant regions in phase space when computing transport rates. Indeed, the ability to obtain accurate pictures of the geometry of phase space has applications to a variety of celestial mechanical problems.

To construct a Poincaré section plot, we select a two-dimensional region $R = \{(x, y, \dot{x}, \dot{y}) : C(x, y, \dot{x}, \dot{y}) = constant, q^i = constant\}$, where $q^i \in \{x, y\}$. We cover a portion of R with a rectangular grid of points and then integrate each point forward in time, recording its position in phase space every time it intersects R. A projection of the recorded positions onto the $(y, \dot{y})$ plane for $q^i = x$ or the $(x, \dot{x})$ plane for $q^i = y$ yields a Poincaré surface-of-section plot that gives information about the structure of phase space in the selected region.

Appendix Figs. 9-12 show a series of Poincaré section plots generated through the use of variational and Runge-Kutta algorithms with a range of time steps h. In virtually all cases, the variational integrator outperforms the Runge-Kutta method in capturing the geometry of phase space. For small time steps, the methods roughly agree on the structure of the Poincaré section. For larger time steps, resonant tori deteriorate and the plotted region appears almost entirely chaotic with the use of the Runge-Kutta algorithm. With the use of a variational integrator, resonant tori persist for large time steps and regions of chaos and stability are easily distinguishable. Note, however, that in some cases (e.g. Appendix Figs. 10(b) and 11(b)) the resonant regions predicted by the variational integrator differ from those predicted by the resolved
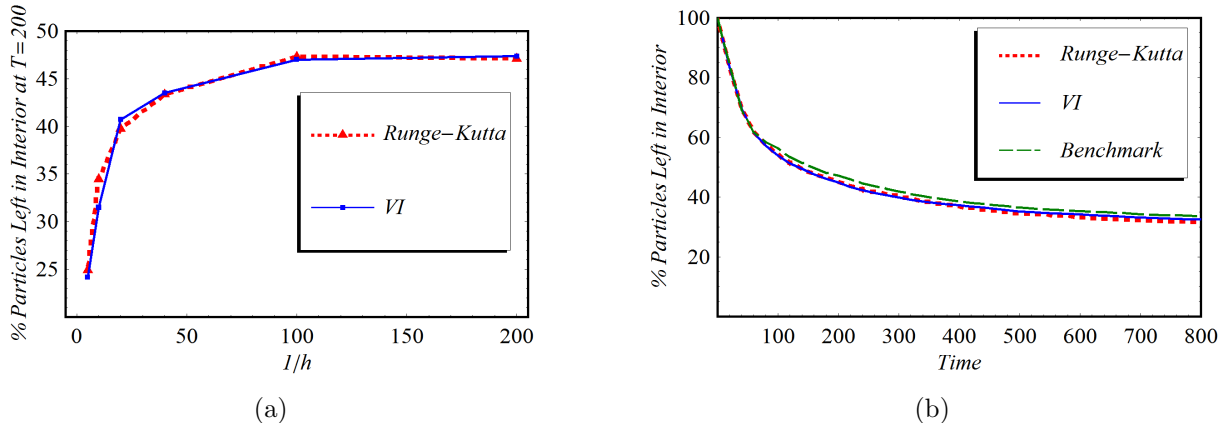
5

Figure 4: (a) Transport rate (interior to exterior) for initial positions uniformly distributed throughout the interior region with $C = 3.004$. Initial velocities were selected such that velocity vectors were oriented counterclockwise at angles nearly perpendicular to their position vectors, with a random deviation angle $\delta \in \left[-\frac{\pi}{4}, \frac{\pi}{4}\right]$ from perpendicular. (b) Transport (interior to exterior) as a function of time for fixed time step $h = 0.01$.

calculation in both their appearance and location, even for small time steps.

The success of variational integrators and other symplectic integrators at producing accurate pictures of the geometry of phase space is not unique to the PCR3BP. Indeed, this phenomenon has been observed for a variety of systems [12,13] and was popularized with a publication by Channel & Scovel [14] in 1990. For an analytical treatment of this topic, see Hairer, Lubich & Wanner [12].

2.4   Transport rates

The study of transport in the three-body problem involves scientists in a surprisingly wide range of fields. For astronomers, an understanding transport phenomena plays a key role in studying asteroid escape rates, collision probabilities, and transport of material throughout the solar system [11,15,16]. On a much smaller scale, transport theory in the three-body problem is of interest to chemists, as it shares an intimate link with reaction rate theory in molecular dynamics [16]. With the growing popularity of implementing theoretical methods to determine transport rates, the need for accurate and computationally inexpensive integration algorithms that can be used to verify theoretical predictions grows accordingly.

In this study, we consider the transport of particles (that are in counterclockwise orbit about the Sun and have a specified energy) from the interior region to the exterior region with respect to the Sun-Jupiter system. As motivation for this analysis, recall from Section 2.3 that for large time steps, the Runge-Kutta algorithm generally gives spurious results when predicting phase space structures: the method predicts chaotic seas where benchmark calculations do not. The presence of additional chaotic regions makes plausible the hypothesis that the Runge-Kutta method is likely to predict excessively high transport rates.

Fig. 4(a) shows the results of Monte-Carlo simulations applied to the above transport problem for various time steps h. The variational integrator and the Runge-Kutta method give nearly indistinguishable results. Both methods give unreliable transport rates with large time steps but appear to asymptotically approach an identical limit. Fixing h and plotting the transport of particles as a function of time (Fig. 4(b)) reveals little more; the two methods give matching results that differ slightly from the benchmark calculation.

Before discarding the suggestion that Runge-Kutta's lack of structure preservation might contribute to erroneous predictions of transport rates, recall that Section 2.2 reveals a case in which Runge-Kutta's energy dissipation leads to changes in the configuration of m_3's allowed regions of motion. It may be that numerical dissipitation is sealing shut the interior region (as shown in Appendix Fig. 6) for some particles in the Monte-Carlo simulation, counterbalancing the influence of Runge-Kutta's introduction of artificial chaos.

6

3   Conclusions and Further Study

Variational integrators were constructed and compared with the fourth-order Runge-Kutta method via application to the PCR3BP. Computational tests verified the superiority of variational integrators over the Runge-Kutta method in conserving energy and producing accurate Poincarè section plots, but revealed no significant differences between the two algorithms' ability to predict individual trajectories and calculate transport rates.

Several components of this study have immediate possibility for further study. From a computational standpoint, introducing adaptive time-stepping schemes to the algorithms would be an appropriate complement to this study. From a celestial mechanical point of view, an extension to three dimensions (removing the restriction that m_3 lie in the orbital plane of the primaries) seems more than fitting. It would also be of interest to further pursue the issue of transport rate simulations; the hypotheses posed in Section 2.4 are still open questions.

4   Methods

4.1   Derivation of the PCR3BP equations of motion

Consider Newton's equations of motion for the full three-body problem in three dimensions:

$$m_1\ddot{\mathbf{r}}_1(t) = \frac{Gm_1m_2}{r_{12}^2}\hat{\mathbf{r}}_{12} + \frac{Gm_1m_3}{r_{13}^2}\hat{\mathbf{r}}_{13} \tag{11}$$

$$m_2\ddot{\mathbf{r}}_2(t) = \frac{Gm_2m_1}{r_{21}^2}\hat{\mathbf{r}}_{21} + \frac{Gm_2m_3}{r_{23}^2}\hat{\mathbf{r}}_{23} \tag{12}$$

$$m_3\ddot{\mathbf{r}}_3(t) = \frac{Gm_3m_1}{r_{31}^2}\hat{\mathbf{r}}_{31} + \frac{Gm_3m_2}{r_{32}^2}\hat{\mathbf{r}}_{32}. \tag{13}$$

Dividing the above equations by m_1, m_2, and m_3, respectively, and letting m_3 approach zero, the equations of motion (11-13) approach

$$\ddot{\mathbf{r}}_1(t) = \frac{Gm_2}{r_{12}^2}\hat{\mathbf{r}}_{12} \tag{14}$$

$$\ddot{\mathbf{r}}_2(t) = \frac{Gm_1}{r_{21}^2}\hat{\mathbf{r}}_{21} \tag{15}$$

$$\ddot{\mathbf{r}}_3(t) = \frac{Gm_1}{r_{31}^2}\hat{\mathbf{r}}_{31} + \frac{Gm_2}{r_{32}^2}\hat{\mathbf{r}}_{32}. \tag{16}$$

Notice that (14) and (15) are merely the equations of motion for the two-body problem, which can be solved analytically[1]. The problem then reduces to finding the motion of m_3 in the presence of two bodies with prescribed orbits. In particular, if m_1 and m_2 are in circular orbit about their center of mass and the motion of m_3 is restricted to the plane of their orbit, the problem reduces to one with two degrees of freedom, the PCR3BP.

To study the PCR3BP, choose units such that $m_1 + m_2 = 1$, $G = 1$, and $r_{12} = 1$. Let $m_2 = \mu$. Now define a counterclockwise rotating coordinate frame whose origin is at the center of mass of m_1 and m_2 and whose x-axis coincides with the vector $\mathbf{r}_{12}$, with m_2 on the positive x-axis. Under the restriction that m_1 and m_2 have circular orbits, it follows that the angular frequency of this rotating frame is 1 and that the positions of $m_1 = 1 - \mu$ and $m_2 = \mu$ in this coordinate system are $(-\mu, 0)$ and $(1 - \mu, 0)$, respectively. See Fig. 1 for a visual aid.

Let (x, y) denote the position of m_3 in the rotating frame, and let $(\bar{x}, \bar{y})$ denote the position of m_3 relative to an inertial frame whose origin is at the center of mass of m_1 and m_2 and whose axes coincide with those of the rotating frame at $t = 0$. It follows that

$$\begin{pmatrix} \bar{x} \\ \bar{y} \end{pmatrix} = \begin{pmatrix} \cos t & -\sin t \\ \sin t & \cos t \end{pmatrix} \begin{pmatrix} x \\ y \end{pmatrix}. \tag{17}$$

7

Differentiation with respect to t yields

$$\begin{pmatrix} \dot{\tilde{x}} \\ \dot{\tilde{y}} \end{pmatrix} = \begin{pmatrix} \dot{x}\cos t - x\sin t - \dot{y}\sin t - y\cos t \\ \dot{x}\sin t + x\cos t + \dot{y}\cos t - y\sin t \end{pmatrix}. \tag{18}$$

The kinetic energy of m_3 is thus equal to

$$\begin{aligned}
T(x,y,\dot{x},\dot{y}) &= \frac{1}{2}\begin{pmatrix} \dot{\tilde{x}} & \dot{\tilde{y}} \end{pmatrix}\begin{pmatrix} m_3 & 0 \\ 0 & m_3 \end{pmatrix}\begin{pmatrix} \dot{\tilde{x}} \\ \dot{\tilde{y}} \end{pmatrix} \\
&= \frac{1}{2}\begin{pmatrix} \dot{x}\cos t - x\sin t - \dot{y}\sin t - y\cos t \\ \dot{x}\sin t + x\cos t + \dot{y}\cos t - y\sin t \end{pmatrix}^T\begin{pmatrix} m_3 & 0 \\ 0 & m_3 \end{pmatrix}\begin{pmatrix} \dot{x}\cos t - x\sin t - \dot{y}\sin t - y\cos t \\ \dot{x}\sin t + x\cos t + \dot{y}\cos t - y\sin t \end{pmatrix} \\
&= \frac{1}{2}m_3((\dot{x}-y)^2 + (\dot{y}+x)^2). \tag{19}
\end{aligned}$$

The potential energy of m_3 is equal to

$$\begin{aligned}
V(x,y) &= -\frac{Gm_1 m_3}{r_{13}} - \frac{Gm_2 m_3}{r_{23}} \\
&= -\frac{m_3(1-\mu)}{\sqrt{(x+\mu)^2 + y^2}} - \frac{m_3\,\mu}{\sqrt{(x-1+\mu)^2 + y^2}}. \tag{20}
\end{aligned}$$

Substituting $L = T - V$ into the Euler-Lagrange equations (3) and simplifying, we arrive at the equations of motion for m_3:

$$\ddot{x} - 2\dot{y} = x - \frac{(1-\mu)(x+\mu)}{((x+\mu)^2 + y^2)^{3/2}} - \frac{\mu(x-1+\mu)}{((x-1+\mu)^2 + y^2)^{3/2}} \tag{21}$$

$$\ddot{y} + 2\dot{x} = y - \frac{(1-\mu)y}{((x+\mu)^2 + y^2)^{3/2}} - \frac{\mu\,y}{((x-1+\mu)^2 + y^2)^{3/2}}. \tag{22}$$

The right-hand side of equations (21) and (22) can be written as the gradient of an effective potential $\Omega(x,y)$, where[1]

$$\Omega = \frac{x^2 + y^2}{2} + \frac{1-\mu}{\sqrt{(x+\mu)^2 + y^2}} + \frac{\mu}{\sqrt{(x-1+\mu)^2 + y^2}} + \frac{1}{2}\mu(1-\mu). \tag{23}$$

The equations of motion (21-22) for the PCR3BP are then equivalent to (6-7).

4.2 Construction of variatational integrators

To construct a variational integrator that models a mechanical system, we write down an expression $L(q(t),\dot{q}(t))$ that equals the difference between kinetic and potential energies of the system in terms of a set of coordinates q. Variational mechanics tells us that $q(t)$ must extremize the integral $\int_0^T L(q(t),\dot{q}(t))\,dt$ subject to fixed endpoints $q(0)$ and $q(T)$ if it is a solution trajectory of the system. From a discrete standpoint, this is equivalent to extremizing the sum

$$\sum_{k=0}^{N-1} L_d(q_k, q_{k+1}, h) \tag{24}$$

subject to fixed endpoints q_0 and q_N, where $\{q_k\}_{k=0}^N$ is a discrete curve of points that approximates the exact solution $q(t)$, h is a time step, and $L_d(q_k, q_{k+1}, h)$ is an approximation of the action integral over the time interval $[k,(k+1)h]$:

$$L_d(q_k, q_{k+1}, h) \approx \int_{kh}^{(k+1)h} L(q(t),\dot{q}(t))\,dt. \tag{25}$$

It can then be shown[3] that this sum is extremized if

$$D_2 L_d(q_{k-1}, q_k, h) + D_1 L_d(q_k, q_{k+1}, h) = 0 \tag{26}$$

---

[1]By convention, the constant $\frac{1}{2}\mu(1-\mu)$ is added to the effective potential $\Omega(x,y)$ so that a particle at rest at either of the equilateral Lagrange points (equilibrium points in the PCR3BP) has a Jacobi constant $C = 3$.

for every k, where D_i symbolizes the derivative of L_d with respect to the ith argument of L_d. These results, analogous to the Euler-Lagrange equations from variational calculus, are appropriately named the discrete Euler-Lagrange equations. They define a recursive relation for finding q_k from a set of initial conditions (q_0, q_1) that can be used to construct algorithms that model mechanical systems.

To integrate the equations of motion (6-7), three variational integrators were constructed using the discrete least action principle described above. Before detailing their structure, note that the use of a rotating coordinate system generates ambiguity with respect to initial conditions. We shall assume that all initial conditions are given in the form $(\bar{x}(0), \bar{y}(0), \dot{\bar{x}}(0), \dot{\bar{y}}(0))$, i.e. relative to an inertial frame whose axes coincide with the rotating frame at $t = 0$. For algorithms that require initial conditions in the rotating frame format $(x(0), y(0), \dot{x}(0), \dot{y}(0))$, the following relation is used:

$$(\bar{x}(0),\ \bar{y}(0),\ \dot{\bar{x}}(0),\ \dot{\bar{y}}(0)) = (x,\ y,\ \dot{x} - y,\ \dot{y} + x). \tag{27}$$

This equation can be derived by evaluating (17) and (18) at $t = 0$. For algorithms requiring initial conditions with velocities replaced by momenta, we multiply $\dot{\bar{x}}(0)$ and $\dot{\bar{y}}(0)$ by m_3. Note, however, that in all of the algorithms that follow, no recursive relations contain m_3 upon simplification and cancellation of common factors.

The first two programs constructed use explicit variational integrator algorithms derived from the use of a rectangular and trapezoidal quadrature rules. In the PCR3BP, the Lagrangian has the form

$$L(x, y, \dot{x}, \dot{y}) = \frac{1}{2}m_3((\dot{x} - y)^2 + (\dot{y} + x)^2) + \frac{m_3(1 - \mu)}{\sqrt{(x + \mu)^2 + y^2}} + \frac{m_3\,\mu}{\sqrt{(x - 1 + \mu)^2 + y^2}}. \tag{28}$$

To implement a rectangle rule variational inegrator, we choose a discrete Lagrangian that approximates $(\dot{x}, \dot{y})$ with $\left(\frac{q_{k+1} - q_k}{h}\right) = \left(\frac{x_{k+1} - x_k}{h}, \frac{y_{k+1} - y_k}{h}\right)$ and then approximate $\int_{kh}^{(k+1)h} L(q, \dot{q})\,dt$ with the length of the time interval times L evaluated at the left endpoint of the interval:

$$
\begin{aligned}
L_d^r(q_k, q_{k+1}, h) &= hL\left(q_k, \frac{q_{k+1} - q_k}{h}\right) \\
&= h\left(\frac{1}{2}m_3\left(\frac{x_{k+1} - x_k}{h} - y_k\right)^2 + \frac{1}{2}m_3\left(\frac{y_{k+1} - y_k}{h} + x_k\right)^2 - V(x_k, y_k)\right).
\end{aligned} \tag{29}
$$

Here, q is the position vector (x, y). Before proceeding to substitute L_d^r into the discrete Euler-Lagrange equations (26), expand (26) into its component form:

$$\frac{\partial}{\partial x_k}L_d(q_{k-1}, q_k, h) + \frac{\partial}{\partial x_k}L_d(q_k, q_{k+1}, h) = 0 \tag{30}$$

$$\frac{\partial}{\partial y_k}L_d(q_{k-1}, q_k, h) + \frac{\partial}{\partial y_k}L_d(q_k, q_{k+1}, h) = 0. \tag{31}$$

Then define the x-component of m_3's momentum at step k as

$$p_k^x = \frac{\partial}{\partial x_k}L_d^r(q_{k-1}, q_k, h) \tag{32}$$

$$= m_3\left(\frac{x_k - x_{k-1}}{h}\right) - y_{k-1}. \tag{33}$$

Using (30), we can rewrite (32) as

$$p_k^x = -\frac{\partial}{\partial x_k}L_d^r(q_k, q_{k+1}, h). \tag{34}$$

Changing the indices in (32), we can write

$$p_{k+1}^x = \frac{\partial}{\partial x_{k+1}}L_d^r(q_k, q_{k+1}, h). \tag{35}$$

Equations ([34](#)-[35](#)) and their y-component anologues

$$p_k^y = -\frac{\partial}{\partial y_k} L_d^r(q_k, q_{k+1}, h) \tag{36}$$

$$p_{k+1}^y = \frac{\partial}{\partial y_{k+1}} L_d^r(q_k, q_{k+1}, h) \tag{37}$$

form a set of recursive relations that can be used to calculate a trajectory from initial conditions $(x(0), y(0), p^x(0), p^y(0))$. Specifically, we solve the simultaneous equations ([34](#)) and ([36](#)) for x_{k+1} and y_{k+1}, use equations ([35](#)) and ([37](#)) to compute p_{k+1}^x and p_{k+1}^y, and repeat for the desired number of iterations. The curve of points $\{q_k\}_{k=0}^{t_f/h}$ calculated in this fashion automatically satisfies the discrete Euler-Lagrange equations ([30](#)-[31](#)) by virtue of the manner in which p_k^x and p_k^y were defined.

To implement a trapezoidal rule variational inegrator, we choose a discrete Lagrangian which approximates $(\dot{x}, \dot{y})$ with $\frac{q_{k+1}-q_k}{h} = (\frac{x_{k+1}-x_k}{h}, \frac{y_{k+1}-y_k}{h})$ and take a weighted sum of $L(q_k, \frac{q_{k+1}-q_k}{h})$ and $L(q_{k+1}, \frac{q_{k+1}-q_k}{h})$:

$$
\begin{aligned}
L_d^{tr}(q_k, q_{k+1}, h) &= \frac{h}{2} L\left(q_k, \frac{q_{k+1}-q_k}{h}\right) + \frac{h}{2} L\left(q_{k+1}, \frac{q_{k+1}-q_k}{h}\right) \\
&= \frac{h}{2}\left(\frac{1}{2}m_3\left(\frac{x_{k+1}-x_k}{h}-y_{k+1}\right)^2 + \frac{1}{2}m_3\left(\frac{y_{k+1}-y_k}{h}+x_{k+1}\right)^2 - V(x_{k+1}, y_{k+1})\right) \\
&\quad + \frac{h}{2}\left(\frac{1}{2}m_3\left(\frac{x_{k+1}-x_k}{h}-y_k\right)^2 + \frac{1}{2}m_3\left(\frac{y_{k+1}-y_k}{h}+x_k\right)^2 - V(x_k, y_k)\right).
\end{aligned}
\tag{38}
$$

We then use equations ([34](#)-[37](#)) (replacing L_d^r with L_d^{tr}) to calculate a trajectory in the manner described in the previous paragraph.

The final variational integrator constructed uses a midpoint quadrature rule for a discrete Lagrangian defined as follows:

$$
\begin{aligned}
L_d^{mp}(q_k, q_{k+1}, h) &= h L\left(\frac{q_k + q_{k+1}}{2}, \frac{q_{k+1}-q_k}{h}\right) \\
&= h\left(\frac{1}{2}m_3\left(\frac{x_{k+1}-x_k}{h}-\frac{y_k+y_{k+1}}{2}\right)^2 + \frac{1}{2}m_3\left(\frac{y_{k+1}-y_k}{h}+\frac{x_k+x_{k+1}}{2}\right)^2\right) \\
&\quad - h V\left(\frac{x_k+x_{k+1}}{2}, \frac{y_k+y_{k+1}}{2}\right).
\end{aligned}
\tag{39}
$$

Replacement of L_d^r with L_d^{mp} in ([34](#)-[37](#)) leads to equations that cannot be solved for x_{k+1} and y_{k+1} explicitly, as was possible with the rectangle and trapezoidal quadrature rules. We therefore invoke Newton's method at each step to find x_{k+1} and y_{k+1}: we introduce the vector

$$
g(p_k, q_k, q_{k+1}) = \begin{pmatrix} -\frac{\partial}{\partial x_k} L_d^{mp}(q_k, q_{k+1}, h) - p_k^x \\ -\frac{\partial}{\partial y_k} L_d^{mp}(q_k, q_{k+1}, h) - p_k^y \end{pmatrix}
\tag{40}
$$

and the Jacobian matrix

$$
J = \begin{pmatrix} \frac{\partial g_1}{\partial x_{k+1}} & \frac{\partial g_1}{\partial y_{k+1}} \\ \frac{\partial g_2}{\partial x_{k+1}} & \frac{\partial g_2}{\partial y_{k+1}} \end{pmatrix},
\tag{41}
$$

where g_i is the ith component of g. We choose an initial guess q_{k+1} with a rough estimate

$$q_{k+1}(1) = q_k. \tag{42}$$

Then we apply the recursive formula

$$q_{k+1}(n+1) = q_{k+1}(n) - J^{-1}(p_k, q_k, q_{k+1}(n)) g(p_k, q_k, q_{k+1}(n)) \tag{43}$$

until a fixed point is reached. q_{k+1} can then be used in (35) and (37) to find p_{k+1}, and the process begins again at (34).

In the comparisons made between variational integrators and the Runge-Kutta method in Section 2, the trapezoidal variational integrator (38) is compared with the fourth-order Runge-Kutta method (5) using equal time steps h. In doing so, we avoid the use of a computationally expensive implicit method (the midpoint variational integrator) without sacrificing the algorithm's order of accuracy (the rectangle variational integrator is first-order accurate, while the midpoint and trapezoidal variational integrators are both second-order accurate).

5 References

1. Goldstein, H., Poole, C. & Safko, J. *Classical Mechanics* (Addison Wesley, San Fransisco, 2002).

2. Szebehely, V. G. *Theory of Orbits: The Restricted Problem of Three Bodies* (Academic Press, New York, 1967).

3. Marsden, J. E. & West, M. Discrete mechanics and variational integrators. *Acta Numerica* **10**, 357-514 (2001).

4. Lew, A., Marsden, J. E., Oritz, M. & West, M. Variational time integrators. *International Journal for Numerical Methods in Engineering* **60**, 153-212 (2004).

5. Lew, A., Marsden, J. E., Oritz, M. & West, M. An overview of variational integrators. *Finite Element Methods: 1970's and Beyond*, 98-115 (2004).

6. Weisstein, E. W. Runge-Kutta Method. From *MathWorld*–A Wolfram Web Resource. http://mathworld.wolfram.com/Runge-KuttaMethod.html

7. Valtonen, M. & Karttunen, H. *The Three-Body Problem* (Cambridge University Press, Cambridge, 2006).

8. Koon, W. S., Lo, M., Marsden, J. E. & Ross, S. Heteroclinic connections between periodic orbits and resonance transitions in celestial mechanics. *Chaos* **10**, 427-469 (2000).

9. Koon, W. S., Lo, M. W., Marsden, J. E. & Ross, S. D. Dynamical systems, the three-body problem, and space mission design. *International Conference on Differential Equations*, Berlin, 1999, (Fiedler, B., Gröger, K. & Sprekels, J. eds.), World Scientific, 1167-1181 (2000).

10. Marsden, J. E. & Ross, S. D. New methods in celestial mechanics and mission design. *Bulletin of the American Mathematical Society* **43**, 43-73 (2005).

11. Dellnitz, M. *et al.* Transport of Mars-crossing asteroids from the quasi-Hilda region. *Physical Review Letters* **94**, 1-4 (2005).

12. Hairer, E., Lubich, C. & Wanner, G. *Geometric Numerical Integration : Structure-Preserving Algorithms for Ordinary Differential Equations* (Springer Series in Computational Mathematics, Berlin, 2002).

13. Rowley, C. W. & Marsden, J. E. Variational integrators for degenerate Lagrangians, with application to point vortices. *41st IEEE Conference on Decision and Control* 1521-1527 (2002).

14. Channel, P. J. & Scovel, C. Symplectic integration of Hamiltonian systems. *Nonlinearity* **3**, 231-259 (1990).

15. Jaffé, C. *et al.* Statistical theory of asteroid escape rates. *Physical Review Letters* **89**, 011101 (2002).

16. Dellnitz, M. *et al.* Transport in dynamical astronomy and multibody problems. *International Journal of Bifurcation and Chaos* **15**, 699-727 (2005).

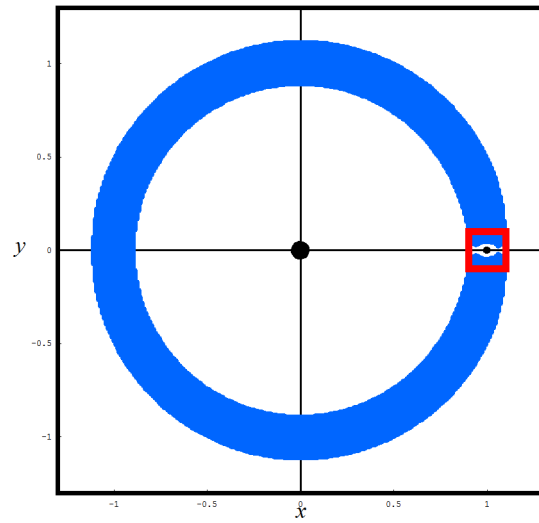# 6   Acknowledgments

7 Appendix

Figure 5: Forbidden regions for energy values in the range of those displayed in Fig. 3, with $\mu = 9.537 \times 10^{-4}$.
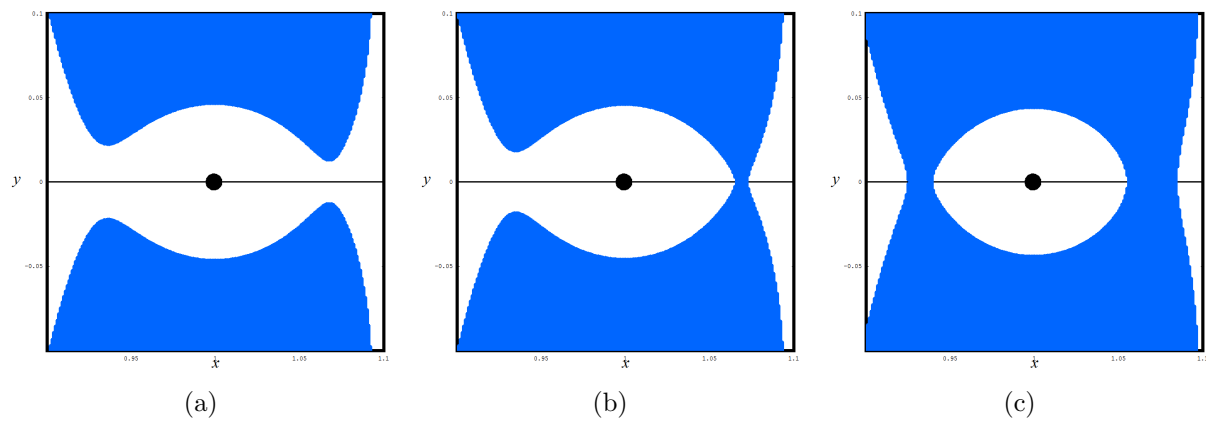

(a)   (b)   (c)

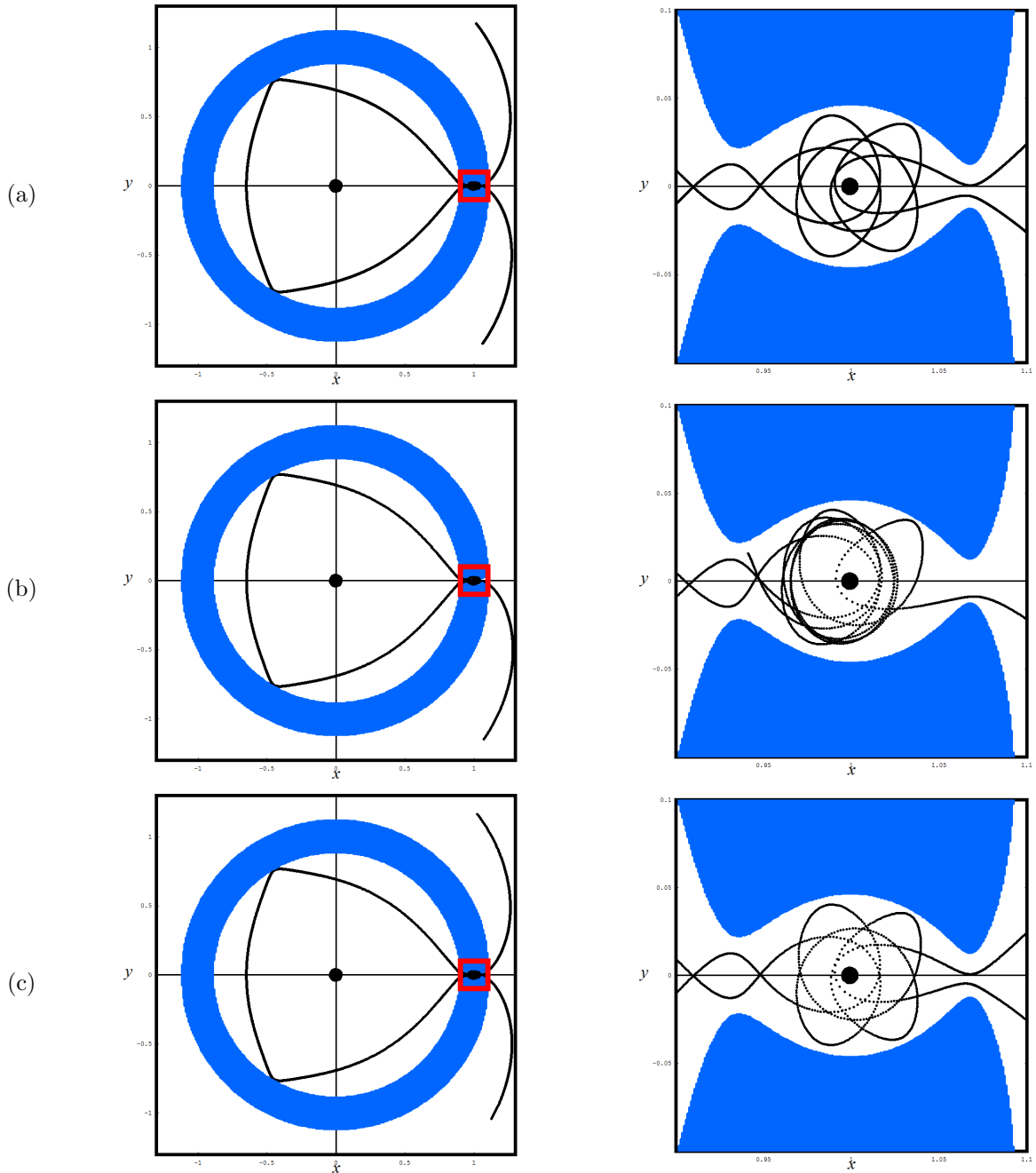Figure 6: Close up of boxed region in Fig. 5 for (a) $E > E_2$, (b) $E_2 > E > E_1$, and (c) $E < E_1$.

13

Figure 7: Transit orbit with initial conditions $x(0) = 1 - \mu$, $y(0) = -0.0190$, $\dot{x}(0) > 0$, $\dot{y}(0) = 0.085$, $C = 3.038$. Both forward and backward integrations of the initial conditions are displayed as single continuous trajectories. Right column shows zoomed views of boxed regions in left column. (a) Benchmark calculation. (b) Variational integrator, $h = 0.01$. (c) Runge-Kutta, $h = 0.01$.
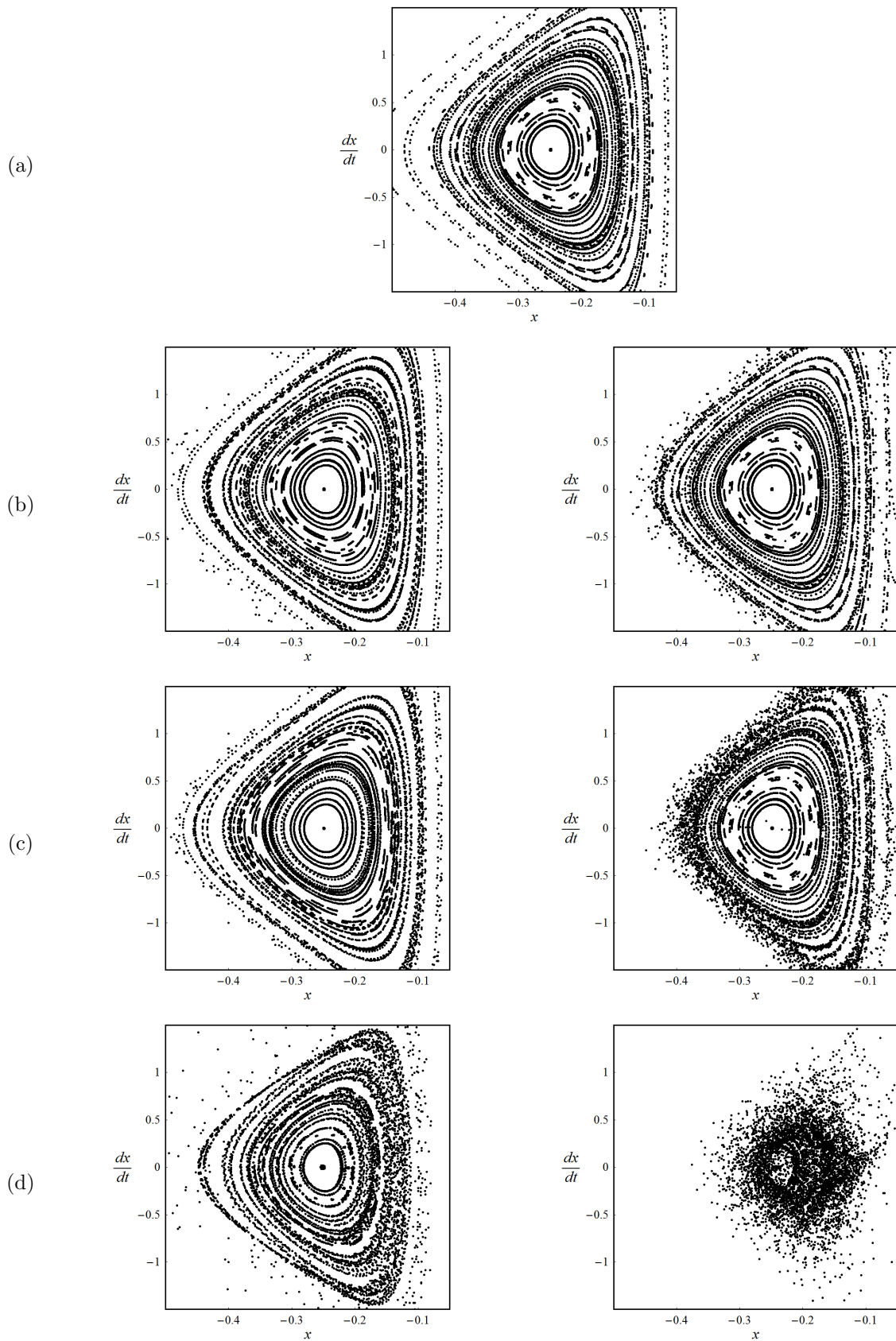
14
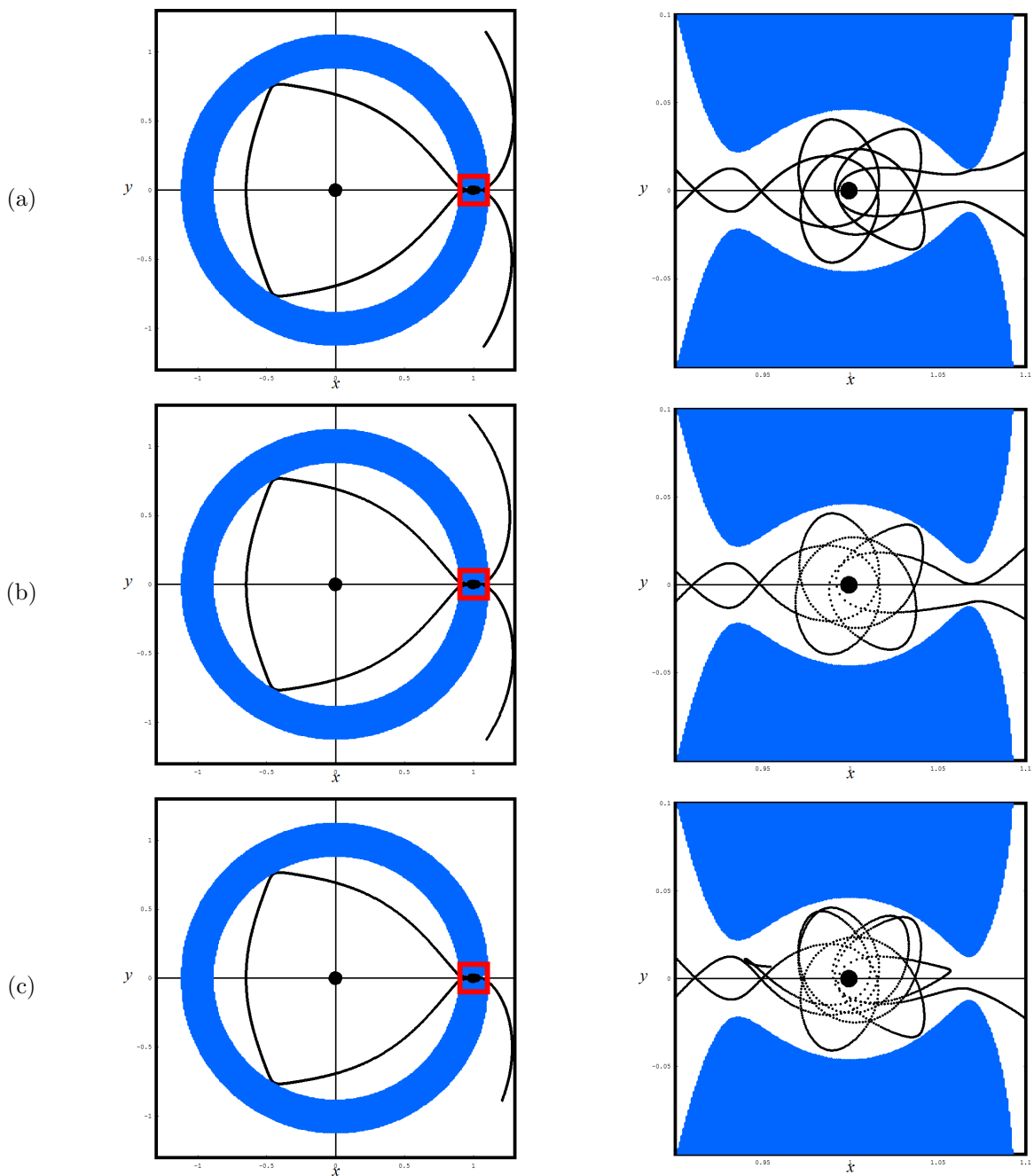
Figure 8: Transit orbit with initial conditions identical to those in Fig. 7, only this time with $y(0) = -0.0192$. Both forward and backward integrations of the initial conditions are displayed as single continuous trajectories. Right column shows zoomed views of boxed regions in left column. (a) Benchmark calculation. (b) Variational integrator, $h = 0.01$. (c) Runge-Kutta, $h = 0.01$.

Figure 9: Poincaré cut at $x < 0$, $y = 0$, with $\dot{y} > 0$, $C = 3.038$. Variational integrator outputs are shown in the left column, while Runge-Kutta outputs are shown in the right column. (a) Benchmark calculation. (b) $h = 0.005$. (c) $h = 0.01$. (d) $h = 0.03$.
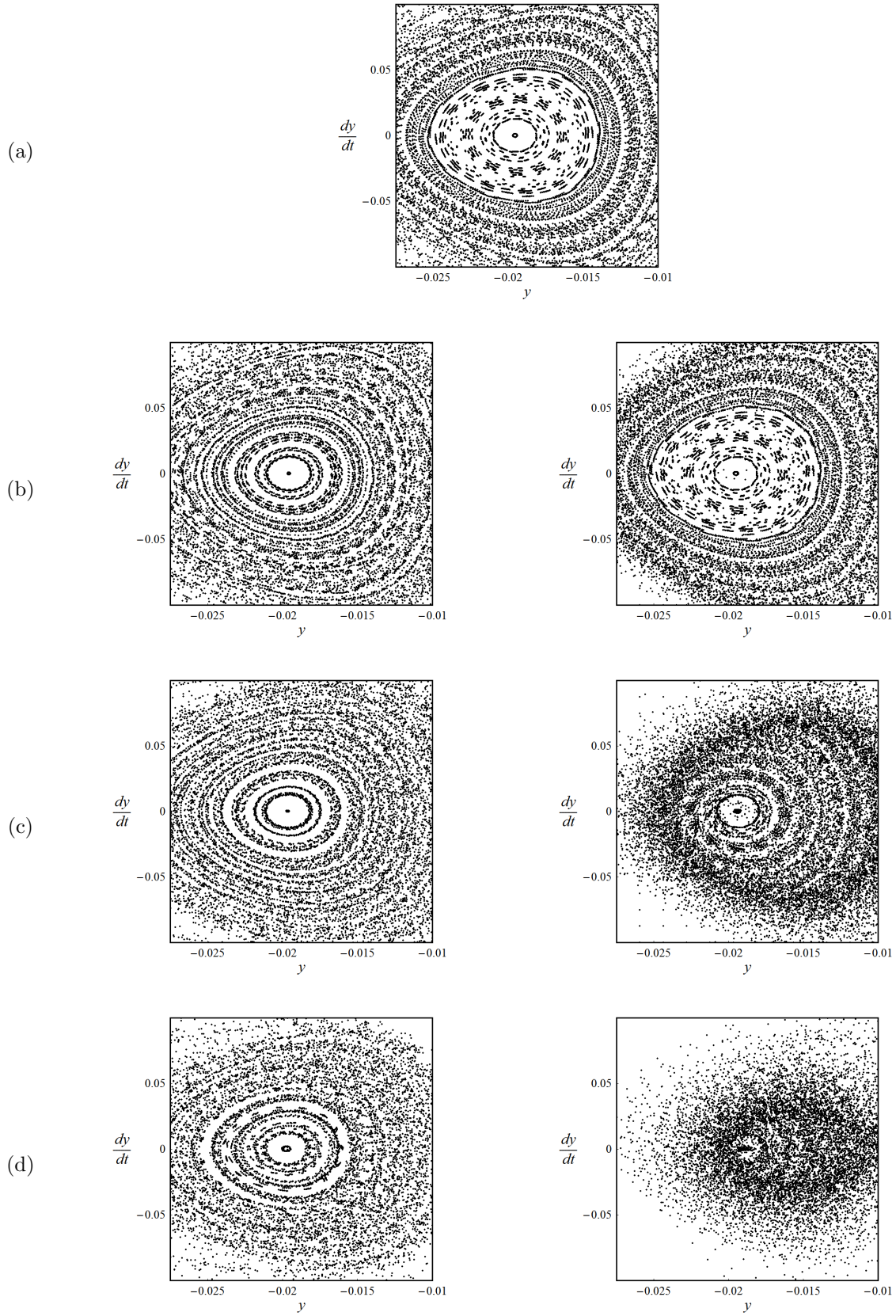
Figure 10: Poincaré cut at $x = 1 - \mu$, $y < 0$, with $\dot{x} < 0$, $C = 3.038$. Variational integrator outputs are shown in the left column, while Runge-Kutta outputs are shown in the right column. (a) Benchmark calculation. (b) $h = 0.01$. (c) $h = 0.0175$. (d) $h = 0.025$.
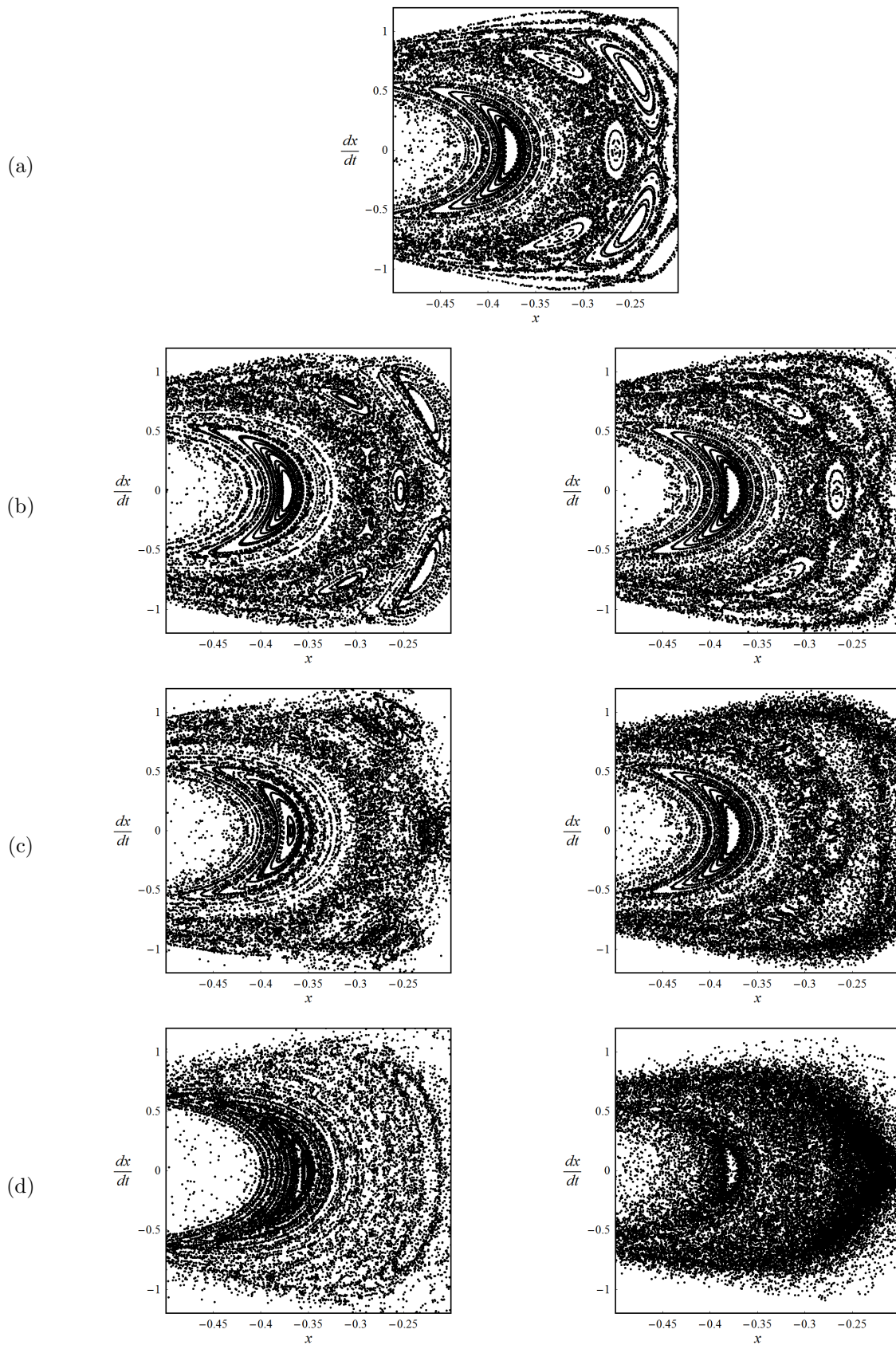
Figure 11: Poincaré cut at $x < 0$, $y = 0$, with $\dot{y} < 0$, $C = 3.038$. Variational integrator outputs are shown in the left column, while Runge-Kutta outputs are shown in the right column. (a) Benchmark calculation. (b) $h = 0.02$. (c) $h = 0.03$. (d) $h = 0.05$.
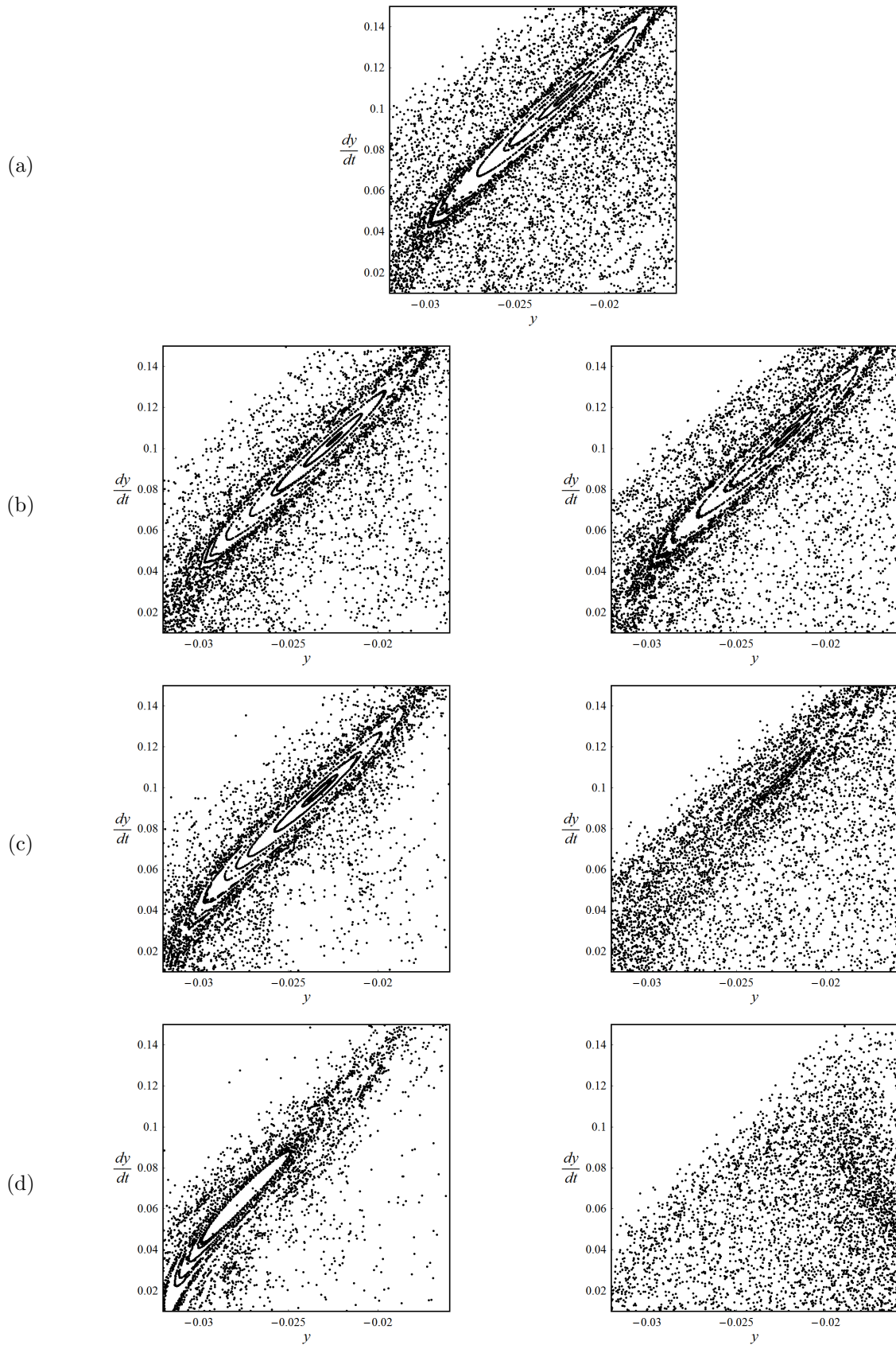
Figure 12: Poincaré cut at $x = 1 - \mu$, $y < 0$, with $\dot{x} > 0$, $C = 3.040$. Variational integrator outputs are shown in the left column, while Runge-Kutta outputs are shown in the right column. (a) Benchmark calculation. (b) $h = 0.005$. (c) $h = 0.01$. (d) $h = 0.025$.